

# Physics of Self-Assembly and Morpho-Topological Changes of *Klebsiella pneumoniae* in Desiccating Sessile Droplets

Abdur Rasheed<sup>1</sup>, Omkar Hegde<sup>1</sup>, Ritika Chaterjee<sup>2</sup>, Srinivas Rao Sampathirao<sup>1</sup>, Dipshikha Chakravortty<sup>2</sup>, Saptarshi Basu<sup>1\*</sup>

<sup>1</sup>Department of Mechanical Engineering, Indian Institute of Science, Bangalore

<sup>2</sup>Department of Microbiology and Cell Biology, Indian Institute of Science, Bangalore

<sup>1</sup>\*Corresponding author<sup>1</sup> email – [sbasu@iisc.ac.in](mailto:sbasu@iisc.ac.in)

<sup>2</sup>Corresponding author email – [dipa@iisc.ac.in](mailto:dipa@iisc.ac.in)

## Abstract

We have investigated the flow and desiccation-driven self-assembly of *Klebsiella Pneumoniae* in the naturally evaporating sessile droplets. *Klebsiella Pneumoniae* exhibits extensive changes in its morphology and forms unique patterns as the droplet dries, revealing hitherto unexplored rich physics governing its survival and infection strategies. Self-assembly of bacteria at the droplet contact line is characterized by order-to-disorder packing transitions with high packing densities and excessive deformations (bacteria deforms nearly twice its original length scales). In contrast, thin-film instability-led hole formation at the center of the droplet engenders spatial packing of bacteria analogous to honeycomb weathering. The varying physical forces acting on bacteria based on their respective spatial location inside the droplet cause an assorted magnitude of physical stress. Self-assembly favors the bacteria at the rim of the droplet, leading to enhanced viability and pathogenesis on the famously known “coffee ring” of the droplet compared to the bacteria present at the center of the droplet residue. Mechanistic insights gained via our study can have far-reaching implications for bacterial infection through droplets, e.g., through open wounds.

## Main

Bacteria orchestrate robust collective responses in dynamic fluid environments by using different physical mechanisms (e.g., suppression of its transport due to fluid shear<sup>1</sup>, oscillatory rheotaxis<sup>2</sup>, swimming against the flow in the wake of curved surfaces/pillars leading to their attachment on the surfaces<sup>3</sup>) that have been developed by evolution over eons. Several recent studies have consolidated the notional importance of the interplay of physical forces in affecting the transport properties of bacteria, their colonization, and survival strategies in novel habitats<sup>4-8</sup>. Unlocking how rugged environments leads to an increase in fitness of the microbes

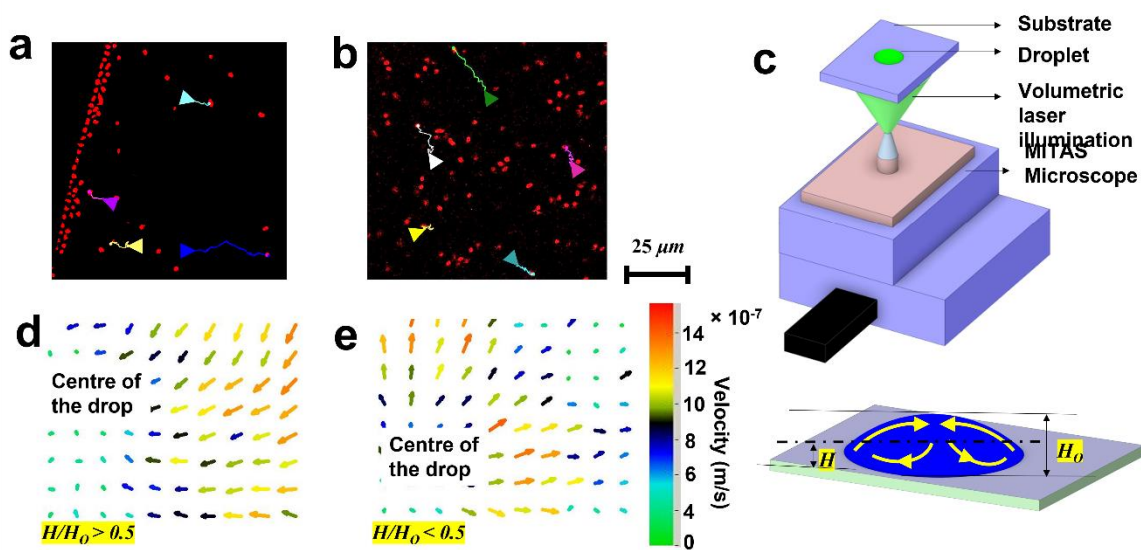
35 may reveal the physical interactions that cause Anti-Microbial Resistance (AMR)<sup>9</sup>.  
36 Opportunistic bacterial pathogens like *Klebsiella Pneumoniae* (KP) are known for their high  
37 frequency and diversity of AMR genes<sup>10-12</sup> and hence are chosen as a model organism in this  
38 study. Besides, bacteria spread through complex transmission routes, for example, through  
39 aerosols<sup>13</sup> and fomites<sup>14</sup>, and are subjected to various physical stresses in wild environments.  
40 Bacteria inside droplets experience several physical stresses<sup>15</sup>, such as shear stress due to fluid  
41 motion in the environment, starvation stress (caused due to lack of nutrients), desiccation stress  
42 (caused due to depletion of water from bacterial cell wall due to evaporation), and stress due  
43 to harsh environmental conditions (fluctuating humidity and temperatures), to name a few. The  
44 bacteria-laden droplets in contact with any surface will eventually evaporate and lead to a  
45 drastic loss in viability of the bacteria<sup>16</sup> due to desiccation at the end stage of evaporation.  
46 However, despite fatal death due to desiccation, few bacteria continue to survive over weeks  
47 on inanimate dry surfaces<sup>17</sup>. Studies show that the final survival of bacteria or even virus in an  
48 evaporating droplet depends on its ability to withstand drying-induced stress<sup>18-20</sup>. The bacteria  
49 on the dried residue of droplets also form patterns, including “coffee rings”; however, motile  
50 bacteria can also alter the deposition patterns by evenly distributing the bacteria on the contact  
51 surface of the dried residue of the droplet<sup>21</sup>. The wettability of the bacterial surface/cell wall  
52 also plays a vital role in forming deposition patterns and the adhesion characteristics on the  
53 surface<sup>22,23</sup>. Order to disorder transition in the coffee ring deposit is observed in both spherical  
54 and rod-shaped inert particles<sup>24,25</sup>. The disordered region is characterized by a random packing  
55 pattern and dispersion in the Voronoi area<sup>26</sup>. However, it is unclear if an active matter like  
56 bacterial cells would exhibit a pattern and trend in packing at the coffee ring.  
57 There are significantly fewer works on the effect of desiccation on the survivability of  
58 bacteria<sup>27-31</sup>. Even these works have only studied what happens to the overall viability without  
59 considering the fate of bacteria (i.e., its morpho-topological changes, the viability variation  
60 within different regions of the deposit, the effect of self-assembly). In the present work, we  
61 will explore how the physical mechanism of self-assembly of KP in evaporating droplets favors  
62 a few bacteria to survive the adverse condition. Investigating the complex patterns formed by  
63 the evaporating droplets containing bacteria that may enhance the survivability and  
64 pathogenesis of bacteria, in the present article, we study the physics pertaining to the self-  
65 assembly-based survivability mechanism of KP in evaporating sessile droplets.

66 **A. Bacterial self-assembly in evaporating droplets**

67 Particle aggregation towards the contact line on pinned sessile droplets evaporating in an  
68 ambient environment is a well-known phenomenon<sup>32</sup>. The colloids suspended in the droplet  
69 are driven along with the flow created to replenish the evaporating water at the edge of the  
70 water droplet, resulting in a coffee ring-type deposition. In contrast, bacterial aggregation is  
71 much more complex than inert particles. For example, bacteria are soft/deformable, have semi-  
72 permeable cell walls, interact, form colonies/combined structures, etc. In addition, droplets  
73 containing bacterial suspension exhibit pinned contact line for the entire evaporation lifetime  
74 on hydrophilic substrates<sup>33-35</sup>.

75 In our experimental set-up, we placed a 1  $\mu$ l droplet of milliQ, suspended with the KP bacteria,  
76 on the clean glass surface, as shown in Fig. 1 (c) (refer to the “Droplet Evaporation” in the  
77 Methods Section for the detailed protocol). As observed from the live-cell imaging, most of  
78 the KP bacteria adsorb at the surface of the droplet (as represented in Fig. 2 (a)) due to the high  
79 electric charge on the bacterial surface (refer to Table 1 in the supplementary information).  
80 Several bacteria faithfully follow the flow inside the droplet, laterally stacking themselves at  
81 the droplet rim (see Video 1, Fig 2. (b)).

82 Although evaporation-driven flow (EDF) inside the droplet exists, all bacteria may often not  
83 faithfully follow the flow<sup>36</sup>. Live-cell imaging reveals the real-time transport of bacteria in the  
84 droplet near the glass surface (at a 10  $\mu$ m distance from the glass surface); Fig. 2 (a) and (b)  
85 show the path line followed by the individual bacteria. Several bacteria move towards the edge  
86 of the droplet; however, few move away from the edge (refer to Fig.1 (a) and Video 1). Few  
87 bacteria in the central region get adhered to the surface and wiggle there, while few others  
88 move in an arbitrary direction. Further, we study the flow inside the droplet to understand its  
89 role in the transport of KP in the droplet. The Micro-Particle Image ( $\mu$ -PIV) Velocimetry  
90 technique is used to quantify the flow inside the droplet, and the schematic representation of  
91 the experimental set-up is shown in Fig.1 (c) (refer to the Methods section for the details of the  
92  $\mu$ -PIV experiment).

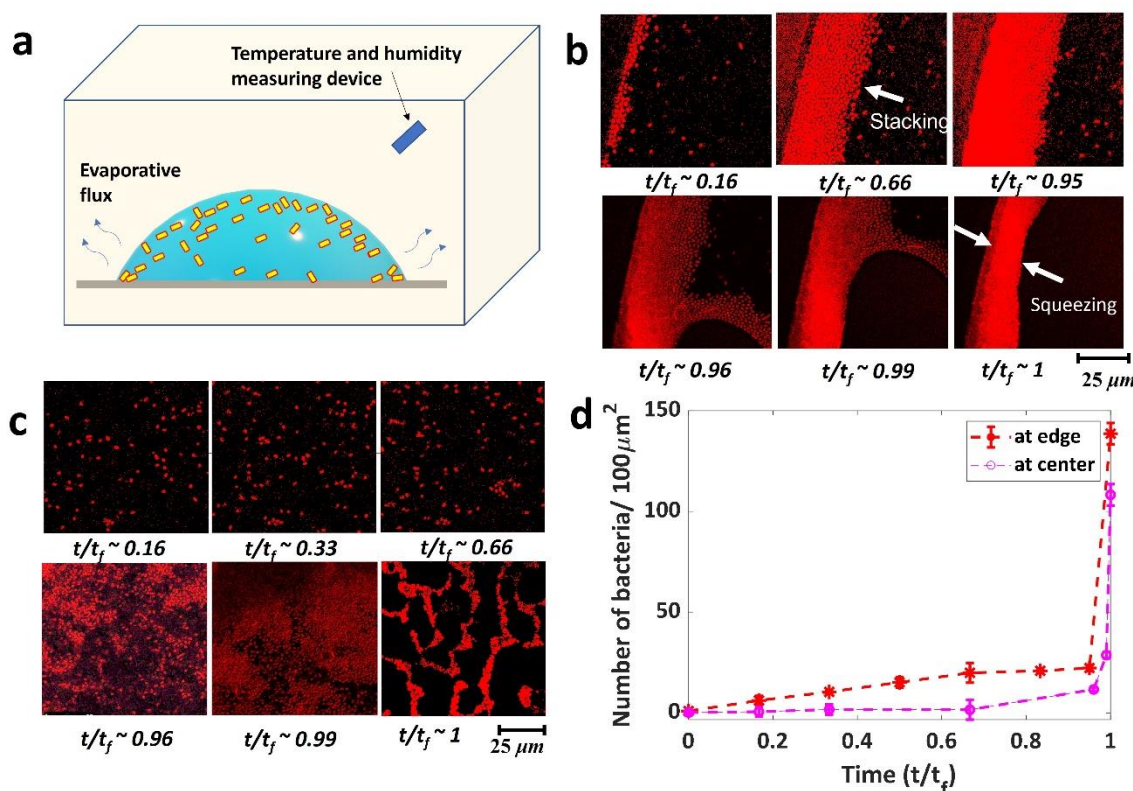


94 **Figure 1 Live Cell tracking of bacteria and hydrodynamics inside the droplet laden with**  
95 **KP. Snapshot of live cell image of the KP suspension droplet (at  $t/t_f \sim 0.1$ ) at the (a) edge**  
96 **of the droplet, (b) center of the droplet. The colored arrows in (a) and (b) show the**  
97 **direction of transport of KP, and the corresponding colored line is the path line followed**  
98 **by the respective bacteria for 10 seconds. (c) Schematic representation of the  $\mu$ -PIV**  
99 **experimental set-up. Vectors of velocity (d) at  $H/H_0 \sim 0.1$  (e) at  $H/H_0 \sim 0.6$ . The scale bar**  
100 **for the velocity vectors for (d) and (e) is adjacent to (e).**

101 Our investigations show circulatory flow in the bacteria-laden Milli-Q water droplet. The flow  
102 is radially inwards (i.e., towards the center of the drop), as shown in Fig.1 (d). Near the glass  
103 surface, the flow is directed radially outwards (see Fig.1 (e)). Since the KP bacteria used in the  
104 experiments are non-motile, the bacteria moving away from the edge of the droplet (in Fig.1  
105 (a)) are, in reality, moving upwards along with the recirculatory flow inside the droplet. Near  
106 the end of evaporation, the bacteria that has not settled in the coffee ring gets deposited in the  
107 rim of the local dewetting hole front, as discussed in section C.

108 As shown in Fig. 2 (b), the ordered packing of KP is similar to the ordering of rod-shaped  
109 particles previously observed by Dugyala et al.<sup>37</sup>. As the height of the droplet becomes thinner,  
110 the evaporative flux at the contact line increases. Subsequently, the flow velocity inside the  
111 droplet towards the contact line also increases. Studies have shown a rapid increase in velocity  
112 near the end of evaporation, usually referred to as ‘the rush hour effect.’ The resulting  
113 deposition at the coffee ring generally exhibits an order to disorder transition<sup>37-39</sup>. We observe  
114 a similar order to disorder transition self-assembly in the case of KP bacteria.

115 The bacterial number density in a region is calculated by considering a region of interest in the  
116 image (for a given instant) and subsequently counting the number of bacteria in the given  
117 region. The values plotted in Fig.2 (d) are the averages of bacterial count in six arbitrary regions  
118 at any given instants, and the error bar corresponds to the standard deviations of the same. This  
119 is scaled/100  $\mu\text{m}^2$  in order to have a substantial number of bacteria for a given region. However,  
120 in the end stage of evaporation ( $t/t_f = 1$ , where  $t$  is the image at any given time instant and  $t_f$  is  
121 the total time of evaporation of the droplet), the bacteria is squeezed and very closely packed  
122 such that it is not possible to obtain the bacterial count in the given region from the live-cell  
123 image. Hence, the bacterial count at  $t/t_f = 1$  is calculated from the Scanning Electron Microscopy  
124 (SEM) images (See Fig.S1 in the supplementary information). It is observed that the bacterial  
125 number density in a given region at the droplet rim increases drastically with time, leading to  
126 very close packing of the bacteria (refer to Fig. 2 (b) and (d)). At the center of the drop, we see  
127 a sudden increase in the visible number of bacteria during the end stages of evaporation. The  
128 focus is adjusted to visualize a section plane of a droplet near the substrate (at a plane 10  $\mu\text{m}$   
129 from the glass surface). Since many bacteria reside near the air-water interface of the drop, as  
130 the drop height reduces, the bacteria move along with the open surface of the droplet towards  
131 the substrate and thus become visible in the live-cell imaging in the end stage of evaporation.



133 **Figure 2 Spatio-temporal dynamics of self-assembly of *Klebsiella Pneumoniae* (KP) in**  
134 **evaporating droplets. (a) Schematic of an evaporating droplet containing the KP bacteria**  
135 **in controlled atmospheric conditions. Temporal sequential live-cell images of KP**  
136 **deposition near the glass surface (at a plane 10  $\mu\text{m}$  from the surface), (b) at the edge, (c)**  
137 **at the center of the droplet. (d) Bacterial count scaled/100  $\mu\text{m}^2$ . For time  $t/t_f=1$ , the**  
138 **bacterial number is counted from the SEM images (as the individual bacteria is not**  
139 **distinguishable in the fluorescence images).**

140 The thin film of liquid and bacteria residue at the end stage of the evaporation of the droplet  
141 ( $t/t_f \sim 0.99$ ) undergoes instability; subsequently, capillary forces dominate, leading to the  
142 formation of holes and compact packing of KP as shown in Fig.2 (c). The bacterial number  
143 density at the center of the droplet residue (for  $t/t_f=1$ ) is calculated from the SEM images in the  
144 region where the bacteria aggregates disregarding the region of holes (see Fig.2 (c)). Fig. 2(d)  
145 shows that the compaction of KP happens in the last one percent of the total evaporation times,  
146 and the self-assembly is dominantly the result of capillary forces and thin-film instabilities at  
147 the end stage of evaporation. This phenomenon in the case of KP is explained in sections C  
148 and D.

149 <sup>36</sup>

150 **B. Ordered to dis-ordered transitions and simultaneous squeezing and buckling of**  
151 **bacteria on “coffee ring”**

152 Based on the type of self-assembly, we have classified the regions within the droplet residue  
153 into three types: 1) ordered region near the edge of the droplet residue – referred to as “Outer  
154 Edge” as shown in Fig.3 (a) and (b). 2) the disordered region – referred to as the “Inner edge”  
155 as shown in Fig.3 (a) and (b). 3) the central region of residue – is referred to as “honeycomb  
156 weathering” Fig.5(a). An aerial view of the bacterial deposits captured from SEM has been  
157 used to analyze the size and bacterial ordering. The bacteria profile is manually marked using  
158 a digital pen to precisely detect the bacterial edges while processing the image (Fig.3 (g)).  
159 ImageJ software is used to binarise the image, and the ‘analyze particle’ plugin is used to get  
160 the size and position characteristics.

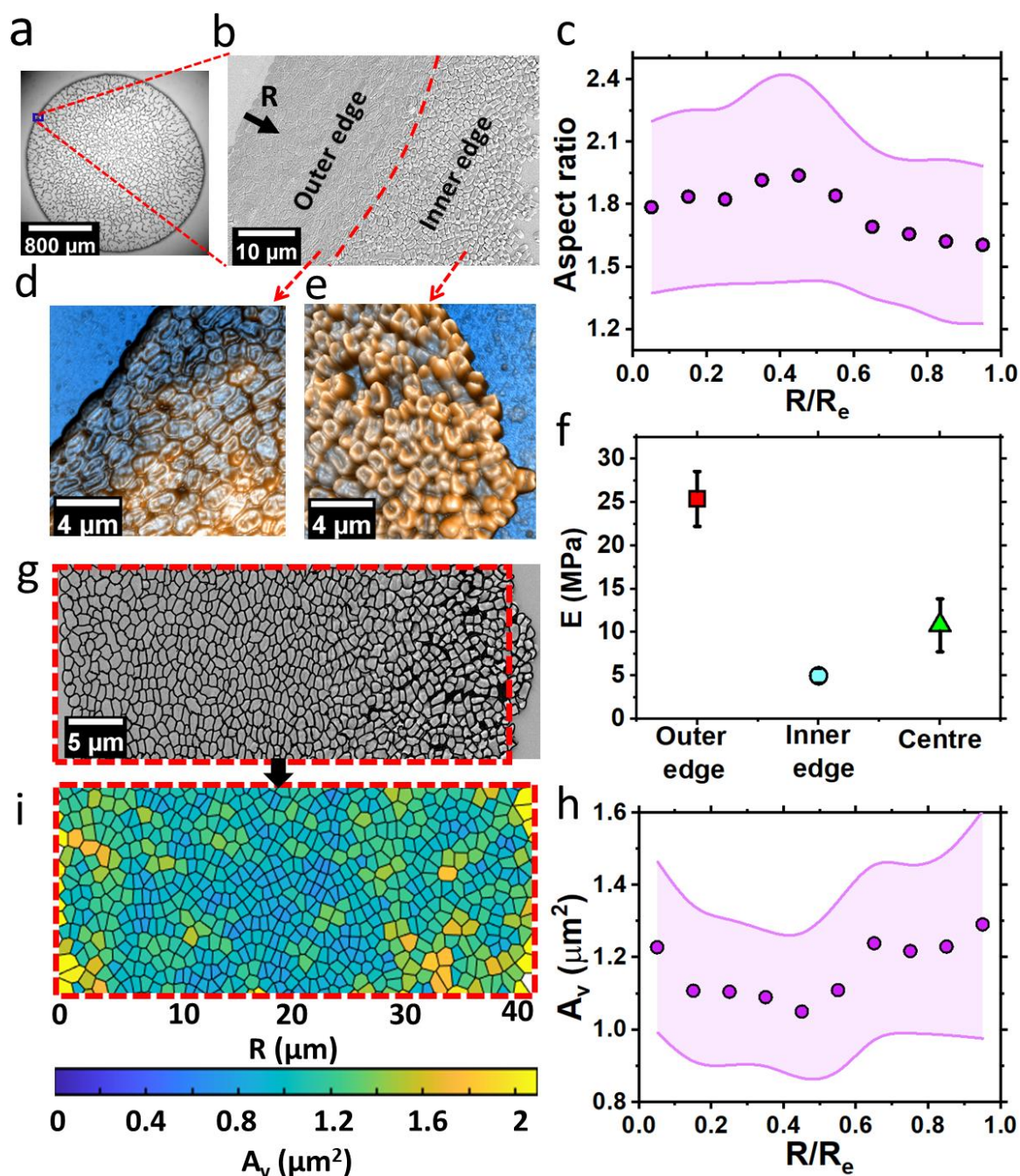
161 We define the maximum and minimum ferret length ratio as the aspect ratio (ratio of length  
162 (L) to the width of the bacteria (W)) of the bacteria. Aspect ratio and vertical height are higher  
163 for the bacteria that got squeezed laterally. The Aspect ratio of bacteria is averaged radially  
164 from the edge (see Fig.3 (b)). The radial distance from the edge, R, is normalized with the

165 thickness of edge deposition (the coffee ring thickness),  $R_e$ . Three different deposits have been  
166 used to get the statistical mean of the plot shown in Fig 3 (c). The deposits from separately  
167 grown cultures have also been tested to ensure repeatability. The aspect ratio is higher at the  
168 outermost edge than in the central region for all the cases. The aspect ratio is highest at  $R/R_e$   
169 between 0.35 to 0.5. Bacteria in this region are highly jammed between the bacteria that settled  
170 at the outermost edge and the incoming bacteria during the rush hour and squeezing effect, as  
171 discussed earlier. The bacteria in the inner edge are in a wide range of aspect ratios depending  
172 on the configuration of the bacteria. Bacteria at the inner edge may be folded due to excessive  
173 desiccation stress and attain U shape<sup>40</sup>.

174 Atomic force microscopy, AFM image (Fig. 3 (d) & (e)) confirms this observation and gives a  
175 clear picture of the bacterial morphology at the inner and the outer edge. The bacteria at the  
176 outer edge are packed with their major axis along the periphery, whereas the bacteria at the  
177 inner edge exhibit a random arrangement. Marin et.al<sup>24</sup>. observed order to disorder transition  
178 in inert sphere particles, and Dugyala<sup>37</sup>et.al<sup>25</sup>. observed this in colloidal rods. The thickness of  
179 the bacterial deposits at the edge varies from 300 nm at the outermost edge up to 700nm in the  
180 highly squeezed region. At the same time, the folded bacteria at the inner edge showed a height  
181 in the range of 350 to 500 nm. Height variation in the outer edge can occur because of variation  
182 in squeezing and water content in bacteria due to variation in the level of desiccation. Whereas  
183 in the inner edge, this variation is due to the degree of folding up of the bacteria, the bacteria  
184 that have folded up more show higher height. Folding of bacteria is a preventive measure to  
185 avoid desiccation. The bacteria try to reduce the exposed area for desiccation by attaining a  
186 coccoidal shape <sup>40</sup>. The bacteria at the inner edge folds because the lateral surfaces are also  
187 exposed for desiccation, unlike the bacteria at the outer edge region enclosed by the closely  
188 packed adjacent bacteria hindering evaporation from its lateral sides. The bacteria at the outer  
189 edge are closely packed, so they are constrained to fold up like those in the disordered region.  
190 Folding is neither seen in the outermost first line of the bacteria on which one of the lateral  
191 surfaces is exposed to the ambient. We hypothesize that the bacterial cell-substrate bonding  
192 might be higher here due to prolonged cell-substrate interaction, which would have prevented  
193 cell folding in the lateral direction.

194 The force-distance spectroscopy analysis done on the bacterial samples through nano  
195 indentation (refer to methods section for details) at various regions in the deposit reveals the  
196 elasticity of the cell membrane of the bacteria. The Modulus of Elasticity (E) of the bacterial  
197 membrane is obtained using the Oliver Pharr model. The results show that the outer edge

198 bacteria are stiffer than the other bacteria. The squeezing effect on these bacteria leading to  
199 very close packing, has increased the stiffness (see Fig. 3 (f)) by nearly one order. E of the  
200 bacteria is  $25 \pm 3$  MPa,  $5 \pm 1$  MPa, and  $11 \pm 3$  MPa at the outer edge, inner edge, and central  
201 region, respectively. The variation in the elasticity modulus can be attributed to the level of  
202 desiccation and ordering dynamics induced gap between the bacteria based on the location.  
203 In addition, the difference in the cross-sectional area normal to the indentation direction would  
204 also be a factor as the bacteria is twice as stiffer in the circumferential direction than in the  
205 axial direction.<sup>41</sup> Deng et al. showed that axial Modulus E =  $23 \pm 8$  MPa, is less than half the  
206 circumferential Modulus E =  $49 \pm 20$  MPa. In the current study, we obtained the elasticity  
207 modulus of the exposed top surface by AFM cantilever tip indentation for all cases. In the case  
208 of outer bacteria lying with their axial direction along the periphery of the droplet deposit, the  
209 top surface indentation gives the circumferential Modulus. The bacterial cross-section in the  
210 axial direction is lesser than in the circumferential direction, and such is



211

212 **Figure 3 Bacterial Self-Assembly at the edge of the droplet.** (a) Optical image of the dried  
 213 residue of the KP droplet. (b) SEM micrograph of the KP deposition at the edge/rim of  
 214 the deposit. (c) The plot of the radially averaged aspect ratio of the bacteria as seen from  
 215 the top view vs. the normalized distance ( $R/R_e$ ) from the outer edge. Where  $R$  is the radial  
 216 distance from the edge of the contact line, and  $R_e$  is the thickness of edge deposition.  
 217 Atomic force microscopy images at the (d) outer edge and the (e) inner edge of the  
 218 precipitate as shown in (b). (f) The plot of the Modulus of Elasticity values ( $E$ ) for bacteria  
 219 at the outer edge, inner edge, and center. (g) SEM micrograph on the edge of the deposit,  
 220 bacteria marked with black border for centroidal Voronoi tessellation processing. (i)

221 **Voronoi cells of the corresponding bacterium shown in. g) color marked according to**  
222 **their size. (h) The Voronoi area of the bacterial deposits was averaged and plotted with**  
223 **normalized distance from the edge  $R/R_e$ .**

224 the elasticity modulus. The inner edge bacterial cross-section gets reduced by folding up, which  
225 decreases elasticity modulus. Correspondingly, we hypothesize, that the bacteria with less  
226 water content is less stiff and deforms more at a given force during indentation. The reasoning  
227 is further supported by the maximum unbinding force (force required to detach the AFM probe  
228 from the sample during retraction) on the indenting probe shown in Fig.S2. The bacteria  
229 deposited at the outer edge show the highest unbinding force (adhesion force) compared to the  
230 bacteria at the other sites. Bacterial cells secrete protein across their membranes upon contact  
231 with other surfaces<sup>42,43</sup>. The variation in adhesion force on the bacterial surface can be attributed  
232 to the secretions from bacterial cells upon interaction with the substrate. Bacterial cells at the  
233 outer edge are in close proximity with the substrate for a longer duration before desiccation,  
234 whereas the bacterium at the central regions gets deposited much later. Shear stress imposed  
235 on the bacteria in different regions could also be an essential factor in expressing adhesive  
236 substances through its membrane which in turn reduces desiccation.

237 The centroidal positions of each bacterium obtained through image analysis are used to study  
238 the bacterial ordering. The bacterial ordering is analyzed by centroidal Voronoi tessellation  
239 using MATLAB. The Voronoi cells in Fig. 3 (i) show the Voronoi area ( $A_v$ ) varying from  $0.5$   
240  $\mu\text{m}^2$  to  $1.85 \mu\text{m}^2$ . The Voronoi area of the cells is obtained by processing the SEM image  
241 Fig.3(g), where the bacterial profile is marked manually for discrete identification of cells. The  
242 average Voronoi area is  $1.1 \mu\text{m}^2$  at the outer edge and  $1.21 \mu\text{m}^2$  at the inner edge. The Voronoi  
243 area reduces inwards in the outer edge region where the bacterium is more squeezed. In  
244 comparison, the Voronoi area increases towards the disordered region. For inert non-  
245 deformable particles, it is observed that the Voronoi area shows a dispersion (sudden increase  
246 in the Voronoi area) from the order to the disordered region<sup>24</sup>. Evidently, such dispersion is not  
247 observed in the bacterial deposition. There could be three causes for this: the squeezing effect  
248 during the hole growth, the capillary force leading to packing during the evaporation of the  
249 mesoscopic thin layer, and the folding of the bacteria.

250 The supplementary Figure ( Fig.S2) shows the overall picture of bacterial deposition at the  
251 edge. The deposit thickness increases from the outer edge and reaches a maximum at  $R/R_e$  of  
252 around  $0.4$  to  $0.5$ . There is a strong relation between the increase in thickness, the decrease in

253 the Voronoi area, and the increase in aspect ratio. The squeezing effect leads to morphological  
254 changes in the bacterial cells resulting in the increment in height and reduction in the area of  
255 contact with the substrate to conserve the volume. Moreover, due to lesser exposed surface area  
256 and desiccation, these bacteria would have more water content and have higher volume than  
257 the edge bacteria and the ones with a gap between them (inner edge). The height variation of  
258 bacterial deposits in the central regions remains less the same, around 200-300 nm(Fig.S3) at  
259 a different location depending on the local ordering of bacteria.

260 **C. Thin-film instability leading to honeycomb weathering**

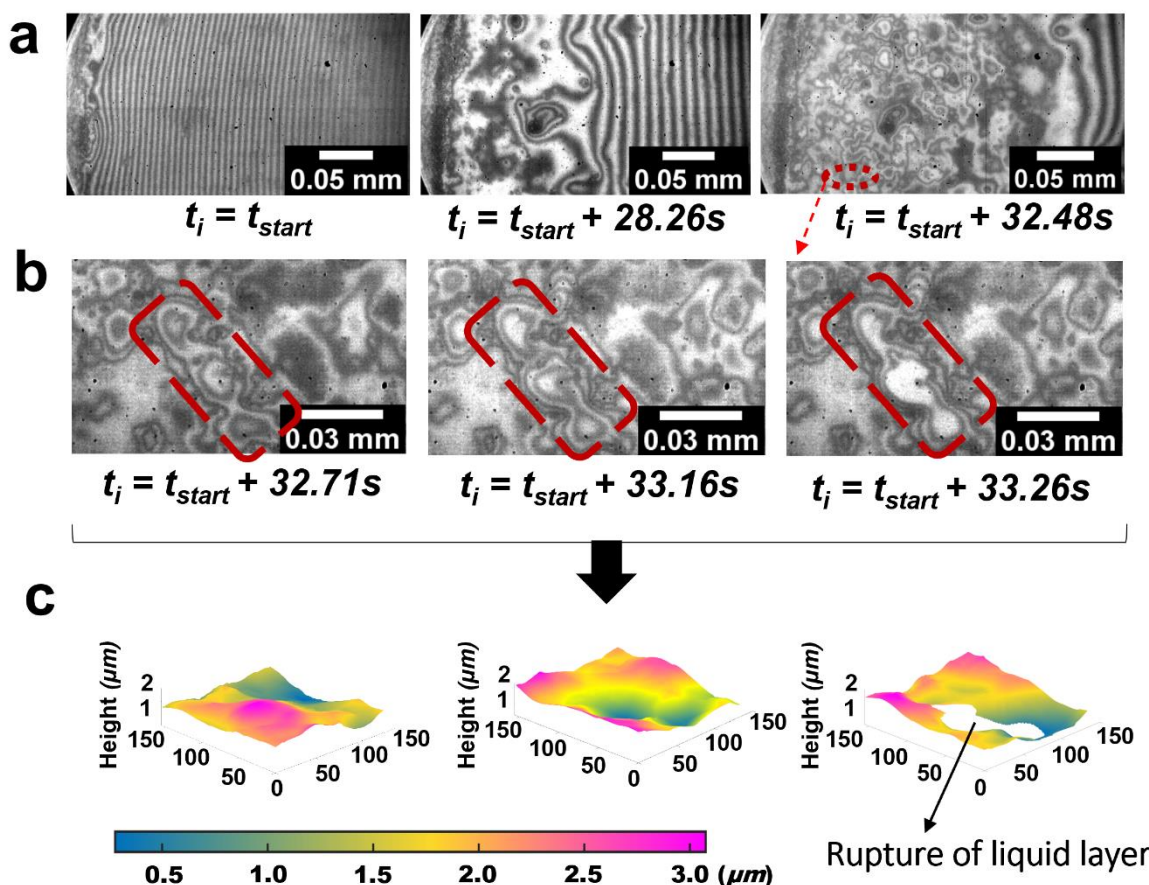
261 Not all bacteria in the droplet get settled at the ring. Depending on the concentration, interface,  
262 and evaporation dynamics, a significant proportion of bacteria would remain dispersed in the  
263 liquid film. In the current study about 50 to 60 % of the bacteria gets deposited on the edge and  
264 the thickness varies from 38 to 44 nm. Liquid thin-film dynamics determine the final deposition  
265 of bacteria not settled in the coffee ring. The perturbations in the liquid thin film would cause  
266 rupture, hole growth, and resulting island formation<sup>44</sup>. The size and shape of these islands  
267 depend on the liquid properties and size, shape, and interfacial properties of the colloids. The  
268 bacteria come closer, leaving a region of low liquid film thickness where the rupture would  
269 occur.<sup>45-47</sup>.

270 The deposition of bacteria in the central regions follows a sequence of events discussed in this  
271 section. At shallow film thickness, the contact line de-pins, leaving a fine mesoscopic layer of  
272 thin liquid film containing bacteria distributed throughout. The depinning is followed by the  
273 thin film instability leading to the cellular pattern formation. Due to thin-film capillary  
274 instability, the liquid film thickness varies along the wetted area. These perturbations get  
275 enhanced due to the presence of bacteria. Fringe patterns were observed as shown in Fig 4 a)  
276 through the reflection interference microscopy at low film thickness. Figure 4 shows the thin-  
277 film variation of the bacteria-laden droplet at various time instants and the phenomena of the  
278 dewetting process of the liquid layer at the conclusive phase of evaporation. Here we take  $t_{start}$   
279 as the time when depinning has started and  $t_i$  is the instantaneous time which is  $t_{start}$  when  
280 depinning has initiated. At the initial time instants ( $t_i = t_{start} + 3.28s$ ), densely spaced fringe  
281 patterns were formed in the form of dark and bright bands, as seen in Fig.4 (a). These patterns  
282 signify the presence of a thicker liquid layer, and from the initial observance of the fringes, the  
283 contact angle of the liquid layer is estimated at approximately  $\approx 5.6^\circ$ . As time progresses, the  
284 fringe width evolves to wider patterns, and instigation of circular patterns of the liquid layer is

285 evident nearer to the contact line of the droplet. The formation of multiple circular patterns in  
286 the liquid layer for ( $t_i \approx t_{start} + 29.20$ ) represents the thinning of the liquid layer compared to  
287 the initial time instants that result in a reduction in thickness of the thin film. The observance  
288 of multiple circular rolls is slightly distant from the leading edge. This phenomenon is  
289 predominant due to the deposition of more bacteria along the droplet's edge.

290 The pinning of droplet without receding the liquid layer consents to the existence of the thin  
291 film. Once the thickness of the thin film is reduced, the evaporation of the liquid layer  
292 surrounding the bacteria elucidates the variation in thickness resulting in the formation of  
293 multiple roll structures and the onset of the dewetting process of the liquid layer. The rupture  
294 of the thin film and the sequence of variation in thickness of the liquid layer at the selected  
295 regions of the initial de-wetting process are presented in Figs 4 (b) and (c). The formation of  
296 multiple rolls at a specific time of 29.43s and adjoining of the rolls in the course time till

297



298

299 **Figure 4 Thin film instability at the center of the droplet. (a) The liquid layer at varying**

300 **time instants during evaporation of the droplet (b) Insights of the de-wetting process in**  
301 **the thin-film layer (c) Variation of the thickness profiles along with the de-wetting**  
302 **phenomena.**

303 the rupture of the thin film is evident from Fig. 4 (b). The rupture of the liquid layer is observed  
304 from the interferometric images at  $t_i = t_{start} + 29.98s$ . The associated two-dimensional  
305 distribution of the height profiles and variation of the thin film was presented in Fig. 4 (c).  
306 During the  $t = 29.43s$ , the presence of multiple rolls (in the selected yellow regions) shows the  
307 increase in the height of the thickness profile, nearly having the maximum height of  $3 \mu\text{m}$ .  
308 In contrast, the adjoining regions of the rolls represent the reduction in thickness variation  
309 nearly to  $1 \mu\text{m}$ . Similarly, at  $t_i = t_{start} + 29.98s$ , the distribution of the height profile surrounding  
310 the rupture region of the liquid layer varied from  $0.5$  to  $1.5 \mu\text{m}$  as the liquid layer recedes to  
311 the adjacent regions. Therefore, the formation of multiple roll-structures (as in  $t_i = t_{start} + 29.20$ )  
312 leads to multiple de-wetting locations regions in the fluid layer, leading to multiple streaks  
313 during the droplet's evaporation (deposition of bacteria) from the droplet edge to the center of  
314 the droplet. Since the droplet de-pining initiates from the edge, the hole formation starts from  
315 the edge. The hole formation progress towards the central region as the film thickness  
316 decreases, as shown in Fig. 5 (a). While the hole near the droplet edge keeps growing, another  
317 hole forms adjacent to the droplet center. The growing front from two holes merges, creating  
318 an island of bacteria.

319 Due to perturbations on the thin film, the hole formations will either increase the surface energy  
320 or decrease it. For a negative change in energy, the hole continues to grow, and for a positive  
321 change in energy, the hole shrinks. Using the energy minimization criterion for a quasi-static  
322 system of hole radius  $r_o$  and inner hole distance  $D$ , the change in energy of a perturbed system  
323  $\Delta E$  can be given as<sup>44</sup>,

$$324 \Delta E = \pi h_{film}^2 \sigma_v \cdot \left[ \frac{-4}{(3+4\ln\rho-4\rho^2+\rho^4)} - \beta \rho^2 \right],$$

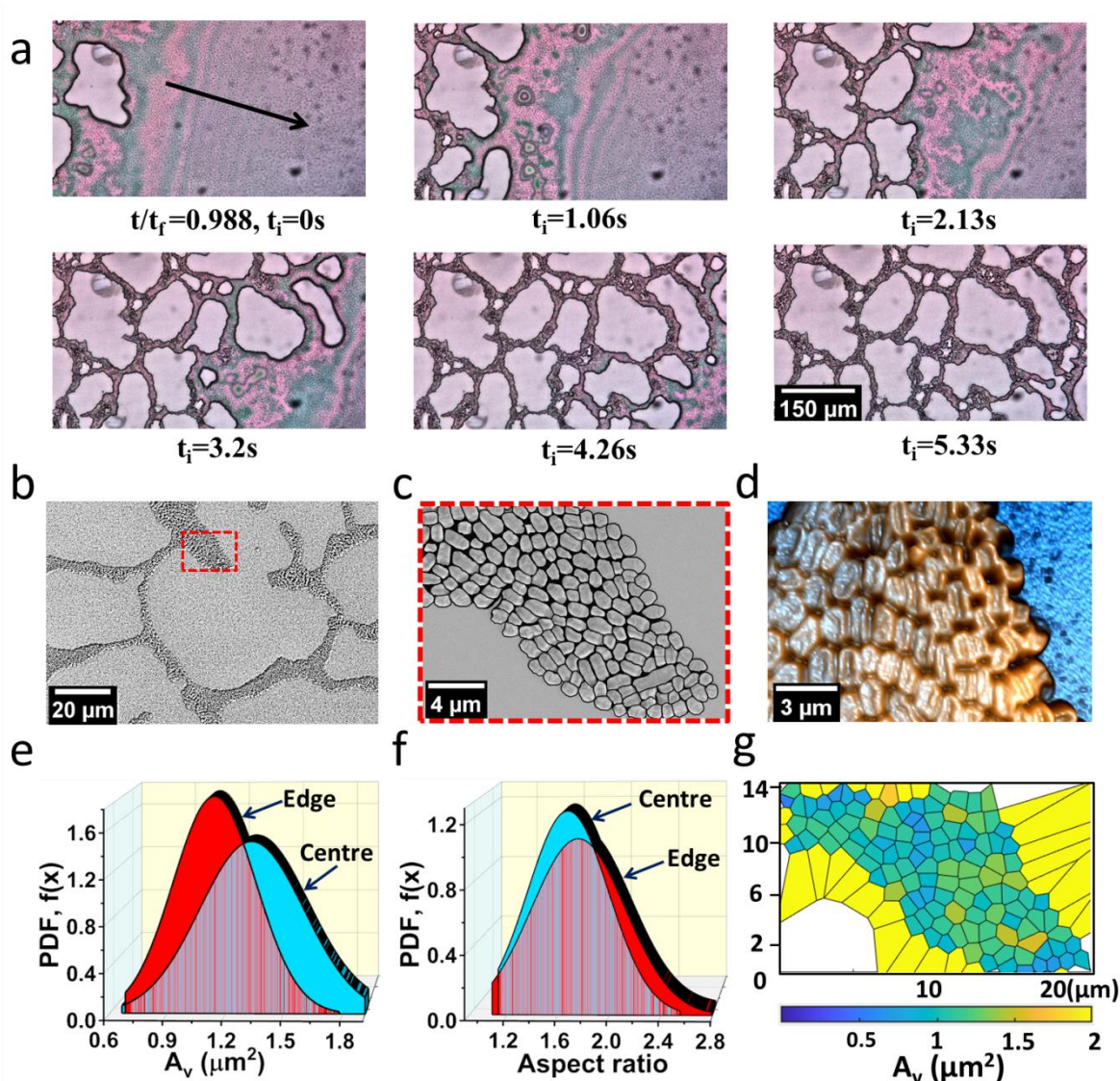
$$325 \text{Where, } \beta = \left( \frac{R}{h_{film}} \right)^2 \cdot (1 + \sigma_s/\sigma_v), \rho = r_o / D$$

326 For  $\beta < 19.5$ , holes of any size will shrink, and the film will become flat. At  $\beta > 500$ , holes will  
327 grow for most of the range of  $\rho$ . Infinitesimally small holes will shrink at any value of  $\beta$ .  $\sigma_v$   
328 represents the film-vapor surface energy  $\sigma_s$ , is the film-substrate surface energy. The major  
329 players in determining the energy change are the hole size, inter-hole distance, and film

330 thickness. At high film thickness, smaller holes produce a positive change in energy, resulting  
331 in shrinking while larger holes could grow. At a film thickness of order  $10 \mu\text{m}$ , holes of size  
332  $r_0 > 3.2 \mu\text{m}$  will create a negative change in surface energy and start to grow in the current case.

333 The instantaneous hole growth at the edge and the central region is compared in Fig.S4 The  
334 pinned contact line, and the edge deposits impede the growth of holes near the coffee ring. The  
335 bacterial cell assembly at the edge is squeezed by the growth of holes adjacent to it. The cells  
336 cannot move further due to the pinning of the contact line. Thus, the hole growth is restricted  
337 toward the coffee ring. However, the holes can still grow towards the center of the droplet. The  
338 normalized hole area exhibits a linear variation in Fig.S4.

339



340

341 **Figure 5 Bacterial Self-Assembly at the central region of the droplet. (a) Spatio-temporal**

342 evolution of the liquid film leading to the rupture and hole growth resembling a cellular

343 pattern (b) SEM micrograph of a cellular structure at the central region (c) Zoomed in

344 SEM micrograph with marked bacterial edge profile, represent the bacterial ordering in

345 the cellular structure (d) AFM image shows the deposited bacterial morphology and self-

346 assembly at the central region (e) Plot comparing the Voronoi Area at the central region

347 to that of the edge of the deposit through Probability density function, PDF,  $f(x)$  plot (f)

348 plot of PDF of aspect ratio (viewed normal to the substrate) of bacteria at the edge and

349 center (g) Color-marked Voronoi cells of the bacterial deposits corresponding to (c).

350 The holes formed at a location further away from the edge can grow with lesser restriction

351 initially. As the adjacent holes start to impinge on each other, growth is slowed down. The

352 normalized hole area variation in the central regions fits very closely to the logarithmic curve

353 (Fig.S3). Here, the growth rate reduces exponentially with time, which shows that the dominant

354 mode in the hole growth mechanism is the surface diffusion<sup>44</sup>. Whereas for the holes near the

355 coffee ring, the growth rate is nearly the same as dictated by the evaporation kinetics<sup>44</sup>. The

356 hole growth rate for an evaporation dominated case is,  $\dot{\rho} = \tan\theta \cdot \frac{A}{h_{film}}$  Where  $\theta$  is the

357 equilibrium wetting angle,  $A$  is the gas-phase transport coefficient, defined as,

358  $p_o \cdot \sigma \cdot \frac{\Omega^2}{(2\pi M)^{1/2} (kT)^{3/2}}$ ,  $p_o$  is the equilibrium vapour pressure on the film surface,  $\sigma$  is the surface

359 energy per unit area of the film/vapour interface,  $\Omega$  is the atomic volume,  $M$  is the atomic

360 weight, and  $kT$  is the thermal energy.  $\dot{\rho} \sim 1\mu\text{m}/\text{s}$  which is of the same order as the growth rate

361 observed in the experiments for the holes. The holes at the central region have an initial velocity

362 two orders higher than that calculated, which drastically reduces to the order of  $1\mu\text{m}/\text{s}$  in less

363 than half the growing time. The total growing time, shape, and size of holes vary randomly.

364 The position of the hole inception, the inter-hole distance, and bacterial density distribution

365 around the hole are the significant factors influencing the final hole size and shape, along with

366 the fluid properties.

367 Habibi et al.<sup>48</sup> studied the pattern of particles in dewetting thin films and proposed a simple

368 model for predicting the dewetting velocity,

369

$$U_{Dewetting} \sim \frac{\sigma}{3\eta} \left( \frac{L_c}{w} \right)^2$$

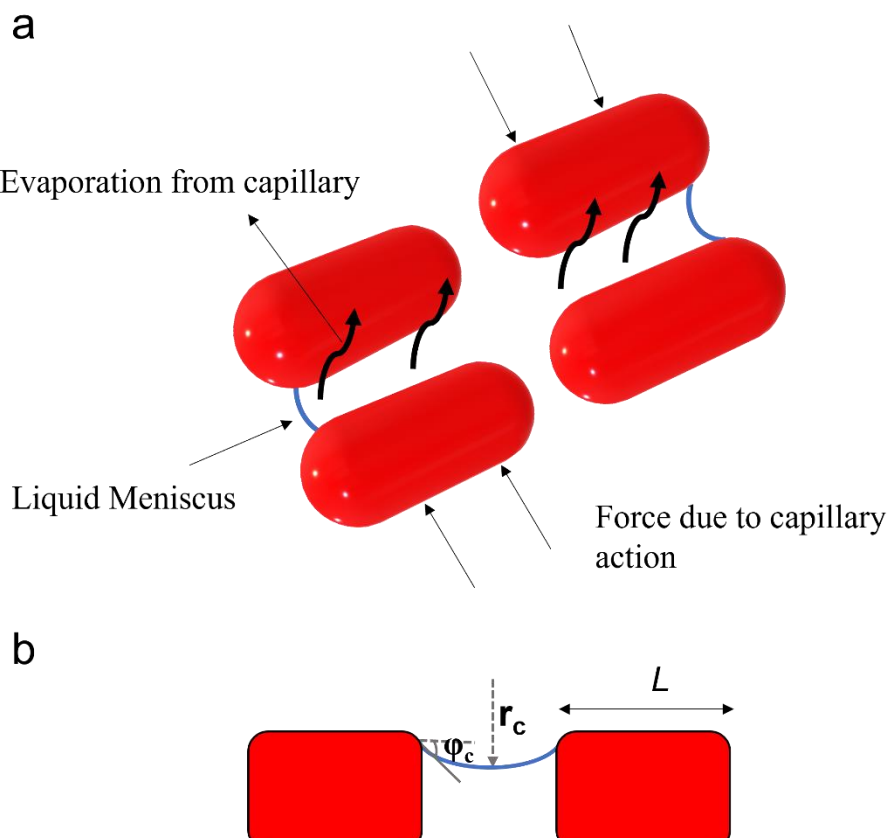
370 Where  $\sigma$  is the surface tension of the liquid film,  $\eta$  is the effective viscosity of the thin liquid  
371 film,  $w$  is the characteristic size of the hole, and  $L_c$  is the bacterial size. The effective viscosity  
372 of the liquid film is a strong function of the volume fraction of bacteria. The Krieger–Dougherty  
373 type law for effective viscosity is  $\eta = \eta_0 (1-\varphi/0.466)^{-2.6}$ , where  $\varphi$  is the volume fraction and  $\eta_0 =$   
374  $10^{-3}$  Pa.s. The equation gives very close values to the effective viscosity calculated using the  
375 above-given formula for dewetting speed<sup>48</sup>. For the wetting velocity of order  $10^{-5}$  m/s and  $10^{-6}$   
376 m/s, the effective viscosity of the medium is 0.0236 Pa.s. and 0.236 Pa.s, respectively. The  
377 corresponding bacterial volume fraction during dewetting is between 0.33 and 0.4. However,  
378 for bacteria, the curve fitting coefficients for calculating effective viscosity would vary, and  
379 there are no studies on the effective viscosity of bacterial solutions at volume fractions more  
380 than 0.1.

381 As shown in Fig. 5 (c), the SEM images are used to analyze the bacterial size and packing. The  
382 AFM image shows that the gap between the bacteria in the central regions is more than that at  
383 the edge. As a result, the Voronoi area of the bacteria aggregates in the central regions is higher  
384 than the edge bacteria aggregates, as shown in Fig. 5 (e). The variation in aspect ratio is nearly  
385 the same for the central and the edge regions. Since the bacteria in the central regions are also  
386 getting squeezed during the hole merging. However, the gap between the bacteria is the cause  
387 of a higher level of desiccation. The bacteria at the rim of the cellular deposits are also folded  
388 like the ones in the inner edges shown in Fig. 5 (d).

#### 389 **D. Mechanistic insights**

390 Along with the dewetting forces, the capillary forces due to the decaying liquid meniscus  
391 between bacteria make the bacteria move closer. Capillary forces led colloidal particle  
392 structuring in thin films is studied by Denkov and Kralchevsky et al.<sup>45,49</sup>. When the liquid film  
393 thickness decreases below the bacterial length scale, the drag force due to liquid flow decreases;  
394 microscopic video (Video 2) shows minimal bacterial movement. During the cellular pattern  
395 formation, the movement of the bacteria is driven by the capillary forces due to varying  
396 meniscus across the bacteria. In partially immersed particles, the deformation of the liquid  
397 meniscus gives rise to interparticle attraction or repulsion. The shape of the liquid meniscus  
398 between the bacteria and the surrounding region determines if the bacteria come closer or are  
399 moving apart. Capillary forces arise due to the pressure and surface effects at the three-phase  
400 contact line inclined at the particle surface. The capillary force of attraction is given by  $F_r = 2\pi$   
401  $\sigma r_c^2 (\sin^2 \varphi_c) (1/L)$  for  $r_c \ll L \ll (\sigma / (\Delta\rho)g)^{1/2}$ , where  $r_c$  is the radius of the three-phase contact

402 line at the bacterial surface,  $\varphi_c$  is mean meniscus slope angle at the contact line,  $\sigma$  is the surface  
403 tension of the liquid film and  $\alpha$  is the contact angle of the bacteria. The distance  $L$  between the  
404 bacteria can be determined by the Laplace equation of capillarity as  $L$  is the length scale of  
405 bacteria.. The capillary force between the bacteria is of the order  $10^{-4}$  N to  $10^{-6}$  N, depending  
406 on the distance between the bacteria.



407  
408 **Figure 6 Mechanistic insights on bacterial aggregation. Schematic representation of (a)**  
409 **formation of a meniscus leading to the capillary attraction between the bacteria at the**  
410 **end stage of evaporation, (b) Side view of the liquid meniscus in between the bacteria**

411 In the central regions, the bacteria do not initially settle down on the substrate because both the  
412 substrate and bacteria are negatively charged (electrostatic repulsion). So, the monolayer of  
413 bacteria would start to form when the thickness of the liquid layer is equal to the size of the  
414 bacteria. The immersion capillary forces between partially immersed bacteria are much higher  
415 than the floatation capillary forces. Thus, the varying meniscus across the bacteria in the film  
416 results in a downward capillary force on the bacteria. At a later stage, the evaporating liquid  
417 between the bacteria alters the liquid meniscus creating an attractive force bringing the bacteria

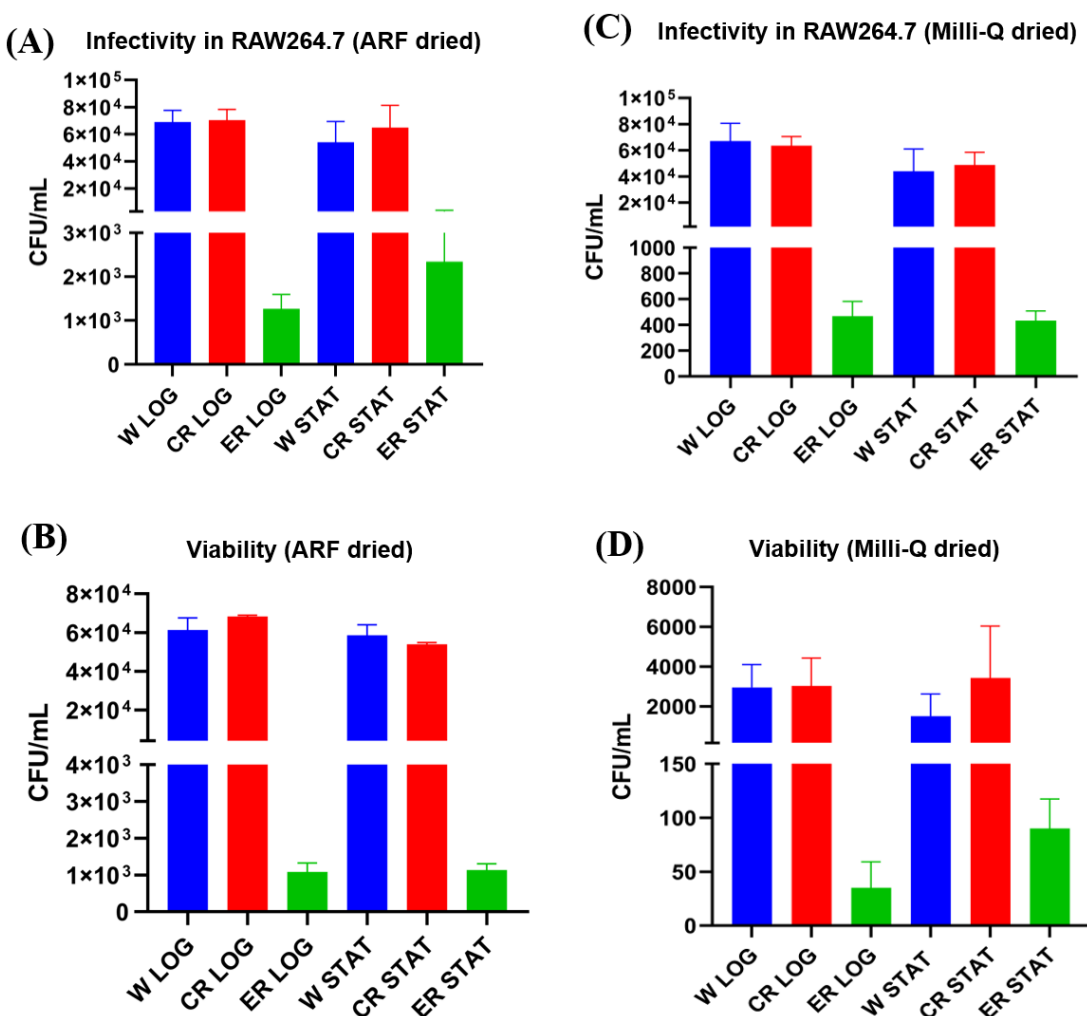
418 together. For the case studied, only a monolayer of deposits has formed. At a higher bacterial  
419 concentration and slower evaporation rate, bilayer and trilayer deposits could form.

420 Fig. S4(a) shows a monolayer deposit of bacteria in the central regions. Malla et al.<sup>50</sup> studied  
421 the effect of particle concentration and particle size on the edge deposition profile. The edge  
422 deposition is either a discontinuous or a continuous monolayer depending on the size of the  
423 particle, for very low particle concentrations below 0.1% v/v and diameter above 1  $\mu\text{m}$ . For  
424 very low bacterial concentrations of less than 0.1% v/v and an effective diameter of more than  
425 1  $\mu\text{m}$  used in this study it is reasonable to obtain a monolayer deposition at the edge. However,  
426 the variation in the thickness (Fig. 4(b)) of the deposition can be attributed to varying levels of  
427 desiccation within the edge deposition and the squeezing.

428

#### 429 **E. Bacterial survivability and pathogenesis aftermath desiccation of the droplet**

430 We studied the survivability and infectivity of bacteria suspended in both Milli-Q water and  
431 surrogate respiratory fluid (SRF). Milli-Q water is used to have a clear visualization of bacteria  
432 which is inhibited in the presence of other colloids such as mucin in real biofluids. To compare  
433 the viability of bacteria in different regions, we scrapped the deposits at the edge keeping only  
434 the central deposits and vice versa. The dried droplet deposits, either whole droplet (W), edge  
435 removed (ER), or center removed (CR), are used for the viability and infectivity studies(refer  
436 to Fig.S5). We observed that the bacterial survival KP was higher in the edge (of the droplet)  
437 deposited bacteria compared to center deposited bacteria, both in the case of bacteria  
438 resuspended in Milli-Q water or SRF. We also observed that the infectivity of the bacterium  
439 deposited at the edge is significantly higher than the center deposited bacteria. This could be  
440 primarily due to the upregulation of virulence genes upon enormous force exerted on the  
441 bacteria during the drying process <sup>51</sup>. We observe these similar observations for both SRF dried  
442 droplet and milliQ dried droplet, suggesting a possible role of physical force on the heightened  
443 virulence of the bacterium.



444

445 **Figure 7 Bacterial survivability and pathogenesis. (A) Infectivity of the bacteria dried in**

446 surrogate respiratory fluid (SRF) droplet in murine macrophages RAW264.7 cells. (B)

447 Viability of bacteria dried in SRF droplet. (B) Infectivity of the bacteria dried in Milli-Q

448 water droplet in murine macrophages RAW264.7 cells. (B) Viability of bacteria dried in

449 Milli-Q water droplet. All experiments are repeated independently three times (N=3);

450 error bars in the plot correspond to the standard error of the mean.

## 451 F. Conclusions

452 The paper compares the nature of bacterial self-assembly, morphology, and viability in drying

453 droplets. The bacterial cells generally die by desiccation. Studies<sup>29,31</sup> have reported that

454 desiccation is an important mechanism by which the bacterial cells in the drying sessile droplet

455 die. This study shows that the self-assembly and desiccation of bacteria suspended in a drying

456 droplet significantly alter the morphology of the bacteria. The bacteria packed closely

457 experience lesser desiccation as their exposed area to the ambient is less. The above discussion

458 serves as the reason why the bacterium at the edge is more viable than that at the central regions.  
459 In real biofluids and saline drying droplets, the increase in salt concentration causes osmotic  
460 shock, driving out water from the bacteria and resulting in death. In contrast, in a hypotonic  
461 solution like pure water used in this study, lysis could cause death. (by water intake and  
462 bursting). If bacteria survive the lytic process, water intake will help sustain the desiccation  
463 process longer than normal bacteria. A typical cellular pattern is formed by bacterial  
464 aggregation in the central region. The thin film instability led to the rupture of the liquid film  
465 causes, hole formation, and growth driving bacteria to come together and form cellular patterns.  
466 However, the gap between the bacteria is more in the central region, and the exposed area for  
467 desiccation is also higher. Thus, lesser viable bacteria are present in the central regions.  
468 Viability studies on realistic biofluids like respiratory fluid droplets also show a similar trend.  
469 A detailed study using actual biofluids is required to understand the phenomena better for  
470 practical applications.

471

## 472 **Methods**

### 473 **Bacterial culture and cell line maintenance:**

474 The bacterial culture of *Klebsiella pneumoniae* (KP) was cultured in Luria Bertani (LB) broth  
475 overnight at 175 rpm shaker and 37°C incubators. The overnight grown (stationary phase)  
476 bacteria were washed five times with Milli-Q water to remove any remnants of the LB media  
477 and then resuspended in either Milli-Q water or SRF as mentioned in the particular experiment.  
478 For the Log phase, bacterial culture, the bacteria were sub-cultured at 1:33 ratio of bacteria:  
479 fresh media and incubated for 2 hours further at 37°C incubator shakers. For staining with a  
480 membrane dye called FM 4-64, the bacteria from stationary or log phase were incubated at the  
481 ice with dye in milliQ (at a concentration 1 $\mu$ g/mL of FM 4-64) for about 15mins, and bacterial  
482 cells were further washed with Milli-Q to remove excess dye and resuspended in Milli-Q or  
483 SRF as mentioned in a given experiment.

484 Murine macrophages were cultured in Dulbecco's Modified Eagle's Media (DMEM)  
485 containing 10% FBS at 37 °C incubator with 5% CO<sub>2</sub>. 12 hours prior to infection experiments,  
486 cells were seeded in 24 well plate at a confluence of 70-80%.

### 487 **Bacterial Viability and Gentamicin Protection Assay:**

488 The dried droplet, either whole droplet (W), edge removed (ER), or center removed (CR), was  
489 resuspended in PBS, and then the resuspended bacteria were plated onto LB agar to an  
490 enumerated viable bacterial number and was also used to infect in RAW264.7 macrophages,  
491 the cells were then centrifuged at 700rpm to increase the adherence of bacteria to mammalian  
492 cells. Next, the bacteria were incubated at 37°C incubators with 5% CO<sub>2</sub>. The cells were  
493 washed after 30mins with PBS, and media was removed and fresh media added containing  
494 100ug/mL of gentamicin; further, after 1hour, media was removed and fresh media containing  
495 25ug/mL of gentamicin. At 2hours and 16 hours post-infection, the mammalian cells were  
496 lysed and plated onto an LB agar plate to enumerate bacterial numbers at specific timepoints.

497 **Droplet Evaporation:**

498 The Surrogate respiratory fluid is prepared according to the procedure mentioned in Rasheed  
499 et.al.<sup>52</sup> The bacteria suspended in Milli-Q and SRF droplets are casted on the glass substrate  
500 cleaned with Isopropyl alcohol. During the experiments, ambient conditions are maintained at  
501 the relative humidity 50 ± 3% and temperature 27 ± 1°C. Droplets of volume 0.95 ± 0.1 µl are  
502 drop cast on glass substrates cleaned with Isopropyl alcohol. The droplets showed an initial  
503 contact angle of 46 ± 2°; the droplet dries in pinned contact line mode with a wetting diameter  
504 of 2.2 ± 0.07 mm. The bacterial motion and deposition near the end of evaporation are recorded  
505 using the bright and dark field optical method.

506 A bright-field image of the final deposition pattern is recorded using a DSLR camera. Scanning  
507 electron microscopy imaging reveals the finer details of the deposition and the arrangement of  
508 bacteria.

509 **Cell imaging and live tracking**

510 The bacterial motion is tracked using membrane stain FM 4-63 with a excitation/emission  
511 maximum of 515/640 nm at 2.28 fps using a Leica TCS SP8 microscope.

512 **Micro-Particle Image Velocimetry (µ-PIV)**

513 The µ-PIV technique is used to qualitatively and quantitatively study the flow inside droplets.  
514 Neutrally buoyant monodisperse (of size 860 ± 5 nm) fluorescent polystyrene particles are used  
515 for µ-PIV experiments. The polystyrene particles mentioned above were procured from  
516 ThermoFisher Scientific. These fluorescent polystyrene particles are added to the bacteria-  
517 containing liquid at 0.008% by volume. These polystyrene particles faithfully follow the flow

518 as their stokes number is (St)  $St = \frac{\rho_p d_p^2 U_c}{18\mu_f L_c} \sim O(10^{-12}) \ll 1$ . Where,  $\rho_p$  is the particle density,  
519  $d_p$  is the diameter of the particle,  $\mu_f$  is the fluid viscosity,  $L_c$  is the characteristic length scale  
520 (~contact diameter of the droplet),  $U_c$  is the expected velocity scale. The droplet containing  
521 bacteria (non-fluorescent) and polystyrene particles (fluorescent) is volumetrically illuminated  
522 using an Nd: Yag laser (NanoPIV, Litron Laser). Images are captured from the bottom of the  
523 solvent droplet using an Imager Intense camera fitted to a Flowmaster MITAS microscope  
524 [Field of View:  $1000 \times 600 \mu\text{m}^2$ , depth of field:  $28 \mu\text{m}$ ]. The images are acquired at  $1 \text{fps}$  using  
525 a single frame–single pulse technique. The particles move 3-4 pixels in the subsequent frames,  
526 optimal for PIV computation. All images are pre-processed by applying appropriate  
527 background subtraction. Post-processing is done by pair-wise cross-correlation of sequential  
528 single-frame images. The interrogation window is maintained at  $64 \times 64$  pixels for the first  
529 pass and  $32 \times 32$  pixels for the subsequent passes with 50% overlap between two windows.  
530 The instantaneous vector fields thus obtained are temporally averaged (over the time period  
531 pertaining to each regime) to obtain the final velocity vectors. The above post-processing of  
532 images is done using DaVis7.2 software from LaVision GmbH.

### 533 **Atomic force Microscopy**

534 Park NX10 atomic force microscope is used to obtain the images and force distance  
535 spectroscopy analysis. The CONTSCR probe with  $0.2 \text{ N/m}$  stiffness is used for the  
536 measurements. The nanoindentation is done at the speed of  $0.3 \mu\text{m/s}$  for both up and down  
537 directions without holding.

### 538 **Credit statement**

539 Conceptualization: S.B. and D.C.; Methodology: S.B., D.C., A.R., O.H., R.C., S.R.S.;  
540 Investigation: A.R., O.H., R.C., S.R.S.; Visualization: A.R., O.H., R.C., S.R.S.; Funding  
541 acquisition: D.C. and S.B.; Project administration: D.C. and S.B.; Supervision: D.C. and S.B.;  
542 Writing— original draft: A.R., O.H., R.C., S.R.S.; Writing: A.R., O.H., R.C., S.R.S.; editing  
543 and revision: S.B., D.C., A.R., O.H., R.C., S.R.S.

544

### 545 **Data availability statement**

546 All relevant data are within the paper and its Supporting Information files. All materials and  
547 additional data are available from the corresponding author upon request.

548

549

550 **References**

- 551 1. Rusconi, R., Guasto, J. S. & Stocker, R. Bacterial transport suppressed by fluid shear. *Nature Physics* 2014 **10**:3 **10**, 212–217 (2014).
- 552 2. Mathijssen, A. J. T. M. *et al.* Oscillatory surface rheotaxis of swimming *E. coli* bacteria. *Nature Communications* 2019 **10**:1 **10**, 1–12 (2019).
- 553 3. Secchi, E. *et al.* The effect of flow on swimming bacteria controls the initial colonization of curved surfaces. *Nature Communications* **11**, 1–12 (2020).
- 554 4. Vizsnyiczai, G. *et al.* A transition to stable one-dimensional swimming enhances *E. coli* motility through narrow channels. *Nature Communications* 2020 **11**:1 **11**, 1–7 (2020).
- 555 5. Kannan, A., Yang, Z., Kim, M. K., Stone, H. A. & Siryaporn, A. Dynamic switching enables efficient bacterial colonization in flow. *Proceedings of the National Academy of Sciences* **115**, 5438–5443 (2018).
- 556 6. Dalwadi, M. P. & Pearce, P. Emergent robustness of bacterial quorum sensing in fluid flow. *Proceedings of the National Academy of Sciences* **118**, (2021).
- 557 7. Guasto, J. S., Rusconi, R. & Stocker, R. Fluid mechanics of planktonic microorganisms. *Annual Review of Fluid Mechanics* **44**, 373–400 (2011).
- 558 8. Stoodley, P., Lewandowski, Z., Boyle, J. D. & Lappin-Scott, H. M. The formation of migratory ripples in a mixed species bacterial biofilm growing in turbulent flow. *Environ Microbiol* **1**, 447–455 (1999).
- 559 9. Bengtsson-Palme, J., Kristiansson, E. & Larsson, D. G. J. Environmental factors influencing the development and spread of antibiotic resistance. *FEMS Microbiology Reviews* **42**, 68–80 (2018).
- 560 10. Peirano, G., Chen, L., Kreiswirth, B. N. & Pitout, J. D. D. Emerging antimicrobial-resistant high-risk *klebsiella pneumoniae* clones ST307 and ST147. *Antimicrobial Agents and Chemotherapy* **64**, (2020).
- 561 11. Wyres, K. L. & Holt, K. E. *Klebsiella pneumoniae* as a key trafficker of drug resistance genes from environmental to clinically important bacteria. *Current Opinion in Microbiology* **45**, 131–139 (2018).
- 562 12. Landman, D. *et al.* Evolution of antimicrobial resistance among *Pseudomonas aeruginosa*, *Acinetobacter baumannii* and *Klebsiella pneumoniae* in Brooklyn, NY. *Journal of Antimicrobial Chemotherapy* **60**, 78–82 (2007).
- 563 13. Tang, J. W., Li, Y., Eames, I., Chan, P. K. S. & Ridgway, G. L. Factors involved in the aerosol transmission of infection and control of ventilation in healthcare premises. *Journal of Hospital Infection* **64**, 100–114 (2006).
- 564 14. Esteves, D. C. *et al.* Influence of biological fluids in bacterial viability on different hospital surfaces and fomites. *American Journal of Infection Control* **44**, 311–314 (2016).
- 565 15. Majee, S. *et al.* Spatiotemporal evaporating droplet dynamics on fomites enhances long term bacterial pathogenesis. *Communications Biology* 2021 **4**:1 **4**, 1–16 (2021).

588 16. Xie, X., Li, Y., Zhang, T. & Fang, H. H. P. Bacterial survival in evaporating deposited droplets on  
589 a teflon-coated surface. *Applied Microbiology and Biotechnology* **73**, 703–712 (2006).

590 17. Kramer, A., Schwebke, I. & Kampf, G. How long do nosocomial pathogens persist on  
591 inanimate surfaces? A systematic review. *BMC Infectious Diseases* **6**, 1–8 (2006).

592 18. Xie, X., Li, Y., Zhang, T. & Fang, H. H. P. Bacterial survival in evaporating deposited droplets on  
593 a teflon-coated surface. *Applied Microbiology and Biotechnology* **73**, 703–712 (2006).

594 19. Huang, Q., Wang, W. & Vikesland, P. J. Implications of the Coffee-Ring Effect on Virus  
595 Infectivity. *Langmuir* **37**, 11260–11268 (2021).

596 20. Alsved, M. *et al.* Effect of Aerosolization and Drying on the Viability of *Pseudomonas syringae*  
597 Cells. *Frontiers in Microbiology* **9**, 3086 (2018).

598 21. Tugba Andac *et al.* Active matter alters the growth dynamics of coffee rings. *Soft Matter* **15**,  
599 1488–1496 (2019).

600 22. van Loosdrecht, M. C., Lyklema, J., Norde, W., Schraa, G. & Zehnder, A. J. The role of bacterial  
601 cell wall hydrophobicity in adhesion. *Applied and Environmental Microbiology* **53**, 1893  
602 (1987).

603 23. Di Martino, P., Cafferini, N., Joly, B. & Darfeuille-Michaud, A. *Klebsiella pneumoniae* type 3 pili  
604 facilitate adherence and biofilm formation on abiotic surfaces. *Res Microbiol* **154**, 9–16  
605 (2003).

606 24. Marín, Á. G., Gelderblom, H., Lohse, D. & Snoeijer, J. H. Order-to-disorder transition in ring-  
607 shaped colloidal stains. *Physical Review Letters* **107**, (2011).

608 25. Dugyala, V. R. & Basavaraj, M. G. Evaporation of sessile drops containing colloidal rods:  
609 Coffee-ring and order-disorder transition. *Journal of Physical Chemistry B* **119**, 3860–3867  
610 (2015).

611 26. Marín, Á. G., Gelderblom, H., Lohse, D. & Snoeijer, J. H. Order-to-Disorder Transition in Ring-  
612 Shaped Colloidal Stains. *Physical Review Letters* **107**, 085502 (2011).

613 27. Nocker, A., Fernández, P. S., Montijn, R. & Schuren, F. Effect of air drying on bacterial  
614 viability: A multiparameter viability assessment. *Journal of Microbiological Methods* **90**, 86–  
615 95 (2012).

616 28. Alsved, M. *et al.* Effect of Aerosolization and Drying on the Viability of *Pseudomonas syringae*  
617 Cells. *Frontiers in Microbiology* **9**, (2018).

618 29. Xie, X., Li, Y., Zhang, T. & Fang, H. H. P. Bacterial survival in evaporating deposited droplets on  
619 a teflon-coated surface. *Applied Microbiology and Biotechnology* **73**, 703–712 (2006).

620 30. Pazos-Rojas, L. A. *et al.* Desiccation-induced viable but nonculturable state in *Pseudomonas*  
621 *putida* KT2440, a survival strategy. *PLoS ONE* **14**, (2019).

622 31. Greffe, V. R. G. & Michiels, J. Desiccation-induced cell damage in bacteria and the relevance  
623 for inoculant production. *Applied Microbiology and Biotechnology* vol. 104 3757–3770 (2020).

624 32. Deegan, R. D. *et al.* Capillary flow as the cause of ring stains from dried liquid drops. *Nature*  
625 (London) **389**, 827–829 (1997).

626 33. Baughman, K. F. *et al.* Evaporative deposition patterns of bacteria from a sessile drop: effect  
627 of changes in surface wettability due to exposure to a laboratory atmosphere. *Langmuir* **26**,  
628 7293–7298 (2010).

629 34. Ranjbaran, M. & Datta, A. K. Retention and infiltration of bacteria on a plant leaf driven by  
630 surface water evaporation. *Physics of Fluids* **31**, 112106 (2019).

631 35. Agrawal, A., Sinha, S., Mukherjee, R. & Mampallil, D. Dynamics of bacterial deposition in  
632 evaporating drops. *Physics of Fluids* **32**, 093308 (2020).

633 36. Wheeler, J. D., Secchi, E., Rusconi, R. & Stocker, R. Not just going with the flow: The effects of  
634 fluid flow on bacteria and plankton. *Annual Review of Cell and Developmental Biology* vol. 35  
635 213–237 (2019).

636 37. Dugyala, V. R. & Basavaraj, M. G. Evaporation of sessile drops containing colloidal rods:  
637 Coffee-ring and order-disorder transition. *Journal of Physical Chemistry B* **119**, 3860–3867  
638 (2015).

639 38. Sefiane, K. Patterns from drying drops. *Advances in Colloid and Interface Science* **206**, 372–  
640 381 (2014).

641 39. Marín, Á. G., Gelderblom, H., Lohse, D. & Snoeijer, J. H. Order-to-disorder transition in ring-  
642 shaped colloidal stains. *Physical Review Letters* **107**, 085502 (2011).

643 40. Cefalì, E. *et al.* *Morphologic Variations in Bacteria under Stress Conditions: Near-Field Optical*  
644 *Studies.* vol. 24 (2002).

645 41. Deng, Y., Sun, M. & Shaevitz, J. W. Direct measurement of cell wall stress stiffening and turgor  
646 pressure in live bacterial cells. *Physical Review Letters* **107**, 7–10 (2011).

647 42. Green, E. R. & Mecsas, J. Bacterial Secretion Systems: An Overview. *Microbiology Spectrum* **4**,  
648 (2016).

649 43. Hooda, Y. *et al.* Slam is an outer membrane protein that is required for the surface display of  
650 lipidated virulence factors in *Neisseria*. *Nat Microbiol* **1**, 16009 (2016).

651 44. Jiran, E. & Thompson, C. v. Capillary instabilities in thin films. *Journal of Electronic Materials*  
652 **19**, 1153–1160 (1990).

653 45. Velev, O. D. *et al.* Mechanism of formation of two-dimensional crystals from latex particles on  
654 substrata. *Progress in Colloid & Polymer Science* **93**, 366–367 (1993).

655 46. Sur, J. & Pak, H. K. Capillary force on colloidal particles in a freely suspended liquid thin film.  
656 *Physical Review Letters* **86**, 4326–4329 (2001).

657 47. Jr, T., J Opt, J. W., Denkov, N. D., Velev A Kralchevsky I B Ivanov, D. P. & Yoshimura Nagayama,  
658 H. K. Two-dimensional crystallization Checkpoint check. *Nagayama, K. Nanobiology* **44**, 25–37  
659 (1954).

660 48. Habibi, M., Moller, P., Fall, A., Rafai, S. & Bonn, D. Pattern formation by dewetting and  
661 evaporating sedimenting suspensions. *Soft Matter* **8**, 4682–4686 (2012).

662 49. Kralchevsky, P. A. & Denkov, N. D. Capillary forces and structuring in layers of colloid  
663 particles. *Current Opinion in Colloid and Interface Science* **6**, 383–401 (2001).

664 50. Malla, L. K., Bhardwaj, R. & Neild, A. Analysis of profile and morphology of colloidal deposits  
665 obtained from evaporating sessile droplets. *Colloids and Surfaces A: Physicochemical and*  
666 *Engineering Aspects* **567**, 150–160 (2019).

667 51. Majee, S. *et al.* Spatiotemporal evaporating droplet dynamics on fomites enhances long term  
668 bacterial pathogenesis. *Communications Biology* **4**, (2021).

669 52. Rasheed, A. *et al.* Precipitation dynamics of surrogate respiratory sessile droplets leading to  
670 possible fomites. *Journal of Colloid and Interface Science* **600**, 1–13 (2021).

671

672